Enhancing the three-dimensional electronic structure in 1111-type iron arsenide superconductors by H substitution

Yoshinori Muraba,[1] Satoru Matsuishi,[2] and Hideo Hosono[1,2,3,*]

[1]*Materials and Structures Laboratory, Tokyo Institute of Technology, 4259 Nagatsuta-cho, Midori-ku, Yokohama 226-8503, Japan*
[2]*Materials Research Center for Element Strategy, Tokyo Institute of Technology, 4259 Nagatsuta-cho, Midori-ku, Yokohama 226-8503, Japan*
[3]*Frontier Research Center, Tokyo Institute of Technology, 4259 Nagatsuta-cho, Midori-ku, Yokohama 226-8503, Japan*

The 1111-type iron arsenide hydride $CaFe_{1-x}Co_xAsH$ was synthesized by high-pressure solid-state reaction, and its electronic structure and superconducting properties were investigated. Bulk superconductivity was observed at $x = 0.09$–0.26. A maximum superconducting critical temperature (T_c^{max}) of 23 K was observed at $x = 0.09$. These values are in agreement with those of $CaFe_{1-x}Co_xAsF$. The calculated Fermi surface of CaFeAsH has a small three-dimensional (3D) hole pocket around the Γ point. This is a result of weak covalent bonding between the As $4p$ and H $1s$ orbitals. No such covalency exists in CaFeAsF, because the energy level of the F $2p$ orbital is sufficiently deep to inhibit overlap with the As $4p$ orbital. The similar superconductivities of $CaFe_{1-x}Co_xAsH$ and $CaFe_{1-x}Co_xAsF$ are explained with the nesting scenario. The small 3D hole pocket of $CaFe_{1-x}Co_xAsH$ does not significantly contribute to electron excitation. These findings encourage exploration of hydrogen-containing 1111-type iron-based materials with lower anisotropies and higher T_c applicable to superconducting wires and tapes.

I. INTRODUCTION

Since the discovery of superconductivity in $LaFeAsO_{1-x}F_x$ [critical temperature (T_c) = 26 K] [1], the physical properties of several families of iron pnictide superconductors have been extensively investigated [2–7]. $LnFeAsO$ (Ln = lanthanide) [1,8–11] and $AeFeAsF$ (Ae = alkali earth) [12,13], or the so-called 1111-type oxyarsenides and fluoroarsenides, respectively, are typical such families. They possess a ZrCuSiAs-type crystal structure, composed of alternately stacked FeAs anti-fluorite-type conducting layers and LnO/AeF fluorite-type insulating layers. Stoichiometric 1111-type families undergo structural and magnetic transition with decreasing temperature. Superconductivity arises when these transitions are suppressed, by carrier doping of the FeAs layers. Carrier doping modes for these 1111-type families are classified as "direct" and "indirect" doping, according to their substitution sites. The former involves elemental substitutions in FeAs layers, such as cobalt or nickel substitution at iron sites [14–17]. The latter involves aliovalent ion substitutions in LnO/AeF layers, such as substitution at oxygen sites with fluorine.

We recently reported the high-pressure synthesis of the hydrogen-substituted 1111-type compounds $CaFeAsF_{1-x}H_x$ ($x = 0.0$–1.0) [18] and $LnFeAsO_{1-x}H_x$ ($x = 0.0$–0.5) [18–20]. Hydrogen is incorporated as H^- at F^- or O^{2-} sites, in the blocking layers of CaFeAsF or $LnFeAsO$, respectively. The high solubility of hydrogen ($x < 0.5$) in 1111-type oxyarsenides results in a wide superconducting dome of $0.05 < x < 0.4$–0.5. The valence state and ionic radius of hydrogen are close to those of fluorine. However, their solubility toward oxygen and their pressure dependence of T_c are rather different [21]. This implies that the large spatial

spread and softness of hydride electrons lead to different chemical bonding states in 1111-type iron pnictides and the fluoride-1111 material.

In this paper, we report the superconductivity of 1111-type CaFeAsH, which is induced by Co substitution at the Fe site. The maximum $T_c = 23$ K and the extent of the superconductivity (SC) region in the x-T diagram are similar to those of Co-substituted CaFeAsF. The effect of hydrogen on 1111-type iron pnictides is discussed, by comparing the electronic structures of $CaFe_{1-x}Co_xAsH$ and $CaFe_{1-x}Co_xAsF$.

II. EXPERIMENT

$CaFe_{1-x}Co_xAsH$ was synthesized by the solid-state reaction of CaAs, CaH_2, Fe_2As, and Co_2As, using a belt-type high-pressure anvil cell. The specific reaction was

$$CaAs + CaH_2 + (1 - x)Fe_2As + xCo_2As$$
$$\rightarrow 2CaFe_{1-x}Co_xAsH. \tag{1}$$
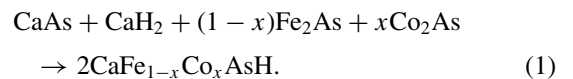
CaH_2, CaAs, Fe_2As, and Co_2As were prepared from their respective metals. CaH_2 was synthesized by heating metallic Ca in a H_2 atmosphere. All starting materials and precursors were prepared in a glove box under a purified Ar atmosphere (H_2O and $O_2 < 1$ ppm). The starting material mixture was placed in a boron nitride (BN) capsule, with a mixture of $Ca(OH)_2$ and $NaBH_4$ acting as an excess hydrogen source [22]. The mixture was heated at 1273 K under 2 GPa for 30 min. The crystal phase and structure were identified by powder x-ray diffraction (XRD), using Mo $K\alpha$ radiation at room temperature. The sample was first ground into a fine powder, and placed in a glass capillary ($\phi = 0.5$ mm). XRD measurements were recorded in transmission mode, to reduce the effects of preferential crystallite orientation. Rietveld refinement of XRD patterns was performed using TOPAS software [23]. The chemical composition was determined by an electron-probe microanalyzer (EPMA; JEOL model JXA-8530F), equipped

---
[*]Corresponding author: FAX: +81-(0)45-924-5196; hosono@lucid.msl.titech.ac.jp

with a field-emission-type electron gun and wavelength dispersive x-ray detectors. Micron-scale compositions within the main phase were probed at ten individual focal points, and the results were then averaged. The temperature dependence of the dc electrical resistivity (ρ) at 2–200 K was measured using the conventional four-probe method, using Ag paste as the electrodes. Magnetic susceptibility (χ) was measured with a vibrating sample magnetometer (Quantum Design). χ was measured on bulk and powdered samples and the data of the powder were adopted. Non-spin-polarized density functional theory (DFT) calculations with Perdew-Burke-Ernzerhof functional [24,25] and the projected augmented plane-wave method [26] were implemented in the Vienna *ab initio* simulation program (VASP) code [27]. A conventional cell containing two chemical formula units, and structural parameters obtained by the interpolation of experimental values, were used. The effect of partial Co substitution at the Fe site was taken into account through the virtual crystal approximation. The plane-wave basis-set cutoff was 600 eV. For Brillouin-zone integrations to calculate the total energy and density of states (DOS), $20 \times 20 \times 10$ Monkhorst-Pack grids of k points were used. The projected density of states (PDOS) was obtained by decomposing the charge density over the atom-centered spherical harmonics with the same Wigner-Seitz radius $r = (3 V_{cell}/4\pi N)^{1/3}$, where V_{cell} and N are the unit-cell volume and number of atoms per unit cell, respectively.

III. RESULTS

A. Crystal structure

Figure 1(a) shows the powder XRD pattern of $CaFe_{1-x}Co_xAsH$, with x value of 0.12. Except for minor peaks arising from Fe metal and unknown impurities, most peaks can be indexed to a ZrCuSiAs-type structure of $P4/nmm$ symmetry, as shown in the inset of Fig. 1(a). Figure 1(b) shows the analyzed x value in $CaFe_{1-x}Co_xAsH$, as a function of (x_{nom}) in the starting mixture. The analyzed x value is proportional to x_{nom}, and its deviation from x_{nom} indicates the segregation of a Co-rich impurity phase. The EPMA analysis indicates the existence of an impurity of composition $CaFe_{1.85\pm0.12}Co_{1.03\pm0.11}As_{1.82\pm0.05}$, in addition to Fe metal. The volume fraction of the Co-rich impurity phase estimated by analyzing the EPMA mapping images (200 μm $\times$ 200 μm, 400×400 points) linearly increases with increasing x and reaches as high as 27% at $x = 0.308$. Figures 1(c) and 1(d) show variations in the $CaFe_{1-x}Co_xAsH$ lattice parameters a and c, respectively, as a function of analyzed x. These parameters for $CaFe_{1-x}Co_xAsF$ are also shown for comparison [28]. The $CaFe_{1-x}Co_xAsH$ a-axis length increases with increasing Co substitution, whereas the c-axis length decreases. The a-axis dimensions of $CaFe_{1-x}Co_xAsH$ are comparable to those of $CaFe_{1-x}Co_xAsF$, whereas the c-axis lengths are ≈ 35 pm shorter than those of $CaFe_{1-x}Co_xAsF$. Figures 1(e)–1(g) show the As distance from the Fe plane (h_{As}), the Ca distance from the H/F plane (h_{Ca}), and the distance between the Ca and As planes (d_{Ca-As}), respectively. While h_{Ca} and d_{Ca-As} remain largely constant, h_{As} decreases with increasing x. This indicates that the monotonic decrease of c-axis length with increasing x originates from the decrease in h_{As}. The different
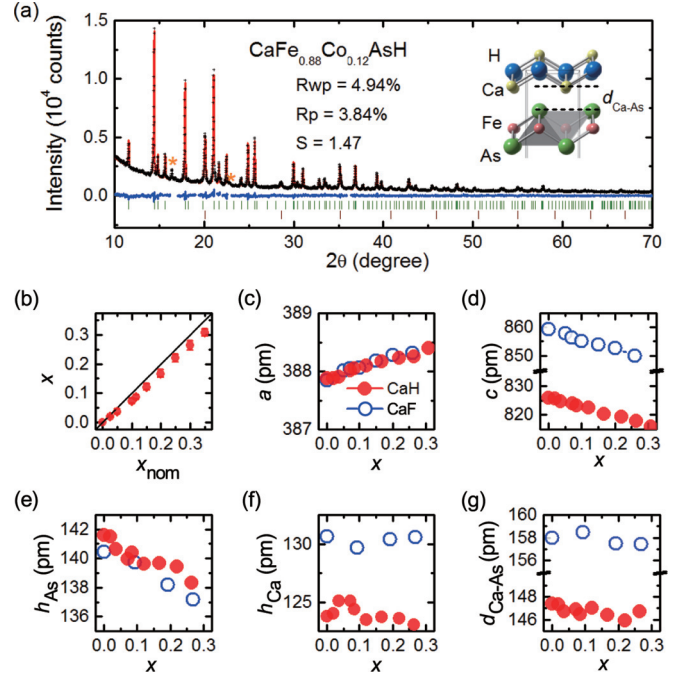

FIG. 1. (Color online) Structural details of $CaFe_{1-x}Co_xAsH$. (a) Powder XRD pattern of $CaFe_{0.88}Co_{0.12}AsH$. Red and black traces indicate observed and Rietveld-fitted patterns, respectively. The differences between them (blue) and Bragg positions of the main phase (green) and Fe impurity (wine red) are also shown. Reflections from unknown phases are denoted by orange asterisks. (b) Analyzed x content as a function of x_{nom}. (c) and (d) Lattice parameters a and c, respectively, as a function of x. (e)–(g) Fe-As bond length, Ca-(H,F) bond length, and distance between the FeAs and blocking layer (d_{Ca-As}), respectively, as a function of x.

h_{As} (<2 pm), h_{Ca} (≈ 7 pm), and d_{Ca-As} (≈ 12 pm) values of $CaFe_{1-x}Co_xAsH$ and $CaFe_{1-x}Co_xAsF$ are independent of Co substitution. This also supports the conclusion that the different c-axis lengths originate from the decrease in d_{Ca-As}.

B. Superconducting properties

Figures 2(a) and 2(b) show the temperature dependence of the electrical resistivity (ρ) for $CaFe_{1-x}Co_xAsH$, with $x = 0.04$–0.12 and 0.17–0.31, respectively. The anomaly in the ρ-T curves due to structural or magnetic transitions is observed at $T_{anom} \approx 80$ K for $x = 0.02$. T_{anom} decreases to ≈ 55 K at $x = 0.04$. These samples exhibit a small ρ decrease at ≈ 20 K, but zero resistivity is not observed. Figures 2(c) and 2(d) show the temperature dependence of the magnetic susceptibility (χ) for $CaFe_{1-x}Co_xAsH$, with $x = 0.04$–0.12 and 0.17–0.31, respectively. The $4\pi\chi$ value of near 0 at $x = 0.02$ and 0.04 indicates that the ρ decrease of these samples arises from the local inhomogeneity of Co. As x increases ≥ 0.07, zero resistivity is attained and the onset T_c reaches a maximum (T_c^{max}) of 23 K at $x = 0.07$. Further Co doping causes a monotonic decrease in T_c. Superconductivity is eventually completely suppressed at $x = 0.31$. Figure 2(e) shows the shielding volume fraction (SVF) evaluated from the gradient of the M vs magnetic field (H) curve at 2 K and the volume fraction of the Co-rich impurity phase estimated
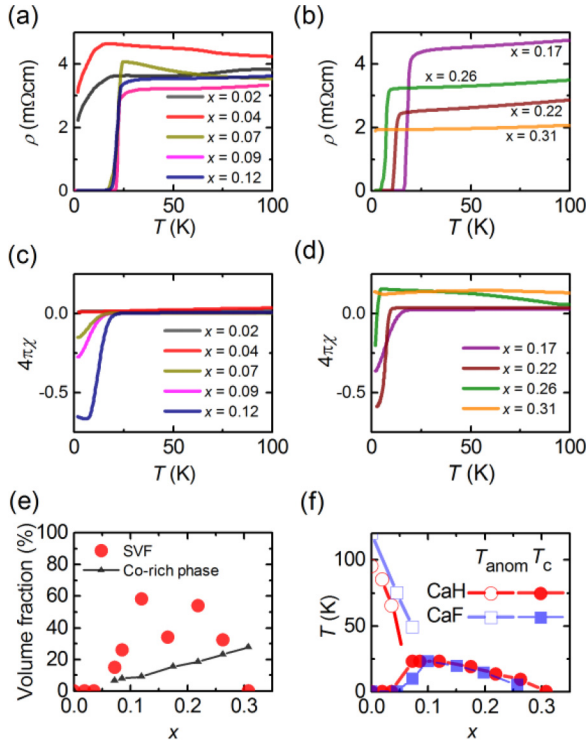
FIG. 2. (Color online) Electronic and magnetic properties of CaFe$_{1-x}$Co$_x$AsH. (a) and (b) ρ-T profiles for x = 0.02–0.12 and 0.17–0.31, respectively. (c) and (d) Zero-field cooling (ZFC) $4\pi\chi$-T curves measured on powdered samples under the magnetic field (H) of 10 Oe for x = 0.02–0.12 and 0.17–0.31. (e) SVF estimated from M-H curves at 2 K and 10 Oe (red circle) and the volume fraction of Co-rich impurity (black line and triangle). (f) x-T diagram of CaFe$_{1-x}$Co$_x$AsH compared with data reported for CaFe$_{1-x}$Co$_x$AsF [28].

by EPMA. The SVF was evaluated by utilizing the volume fraction of contained phases in samples estimated by EPMA on the assumption that the density of the Co-rich impurity phase

was the same as that of CaFe$_2$As$_2$ whose constituent element and composition is very close to the Co-rich impurity phase. The SVF value of $>26\%$ for samples of $0.09 < x < 0.26$ indicates bulk superconductivity. Here, we mention that the possibility of superconductivity derived from the Co-rich impurity. Since there are no steps on the $4\pi\chi$-T curves in the superconducting region, superconductivity observed here is probably caused by a unity phase unless superconducting domes of the others phases accidentally coincide. Moreover, the volume fractions of the Co-impurity phase are smaller than SVF values in the range of $0.09 < x < 0.26$. Consequently, it is concluded that observed superconductivity is caused by CaFe$_{1-x}$Co$_x$AsH. Figure 2(f) shows T_{anom} and T_c^{onset} values from the ρ-T curves, as a function of x. These values for CaFe$_{1-x}$Co$_x$AsF are also shown for comparison [12]. T_c-dome values for CaFe$_{1-x}$Co$_x$AsH are in the range of x = 0.09–0.26, with T_c^{max} = 23 K. The T_c^{max} and the extent of the SC region are comparable to those of CaFe$_{1-x}$Co$_x$AsF. This implies that the superconducting properties are not significantly changed by replacing the F$^-$ blocking layer anion with H$^-$.

C. Electronic structures

Figure 3(a) compares the calculated DOS of CaFeAsF and CaFeAsH. Energy bands located around the Fermi level (E_F) are mainly composed of Fe $3d$ states. The DOS of these two compounds are comparable at $-2 < E < 2$ eV. Below the Fe $3d$ bands, the energy bands are mainly composed of As $4p$ states, which are located at $-6 < E < -2$ eV. In CaFeAsF, fluorine $2p$ states form further bands at $-7.5 < E < -5.5$ eV, without admixing with the orbitals of other atoms. On the other hand, in CaFeAsH, hydrogen $1s$ states energetically overlap well with As-$4p$ states. Ca orbitals contribute at $-2 < E < -5$ eV, which suggests that they admix with the H $1s$ orbital. Figure 3(b) shows band dispersion and the contribution of Fe-$3d$ orbitals. In CaFeAsF, there are three hole pockets around the Γ point, and two electron pockets around the M point. The dispersion and orbital contribution of the electron
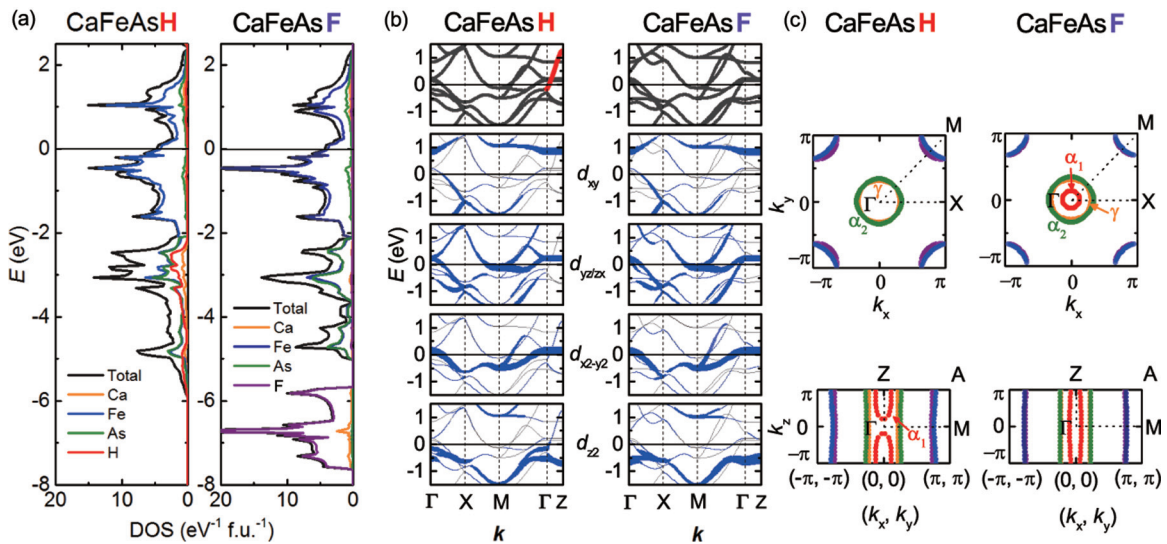

FIG. 3. (Color online) Calculated electronic structures of CaFeAsH and CaFeAsF. (a) Total DOS and PDOS of CaFeAsH (left) and CaFeAsF (right). (b) Band structures along directions of high symmetry in the Brillouin zone. Thick bands (blue) show the amounts of Fe-d_{xy}, $d_{yz/zx}$, $d_{x^2-y^2}$, and d_{z^2} character. (c) Cross sections of Fermi surfaces in the $k_z = 0$ (top) and $k_x = k_y$ (bottom) planes.
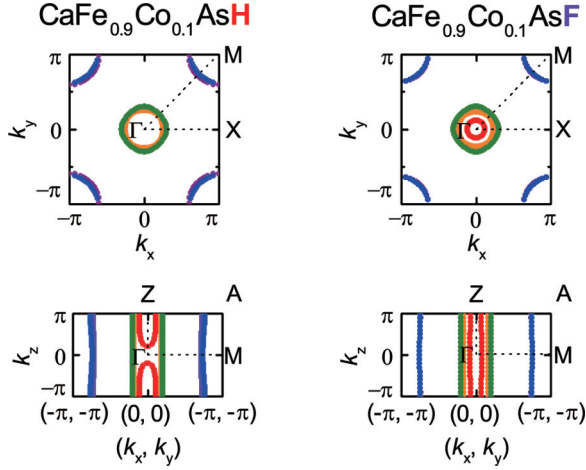
FIG. 4. (Color online) Cross sections of Fermi surfaces of $CaFe_{0.9}Co_{0.1}AsH$ and $CaFe_{0.9}Co_{0.1}AsF$, in the $k_z = 0$ (top) and $k_x = k_y$ (bottom) planes.

pockets and two of the three hole pockets are comparable with those of CaFeAsH. However, one holelike band in CaFeAsH crosses the E_F in the Γ-Z path, as shown by the red line in Fig. 3(b) (which corresponds to the crystallographic c axis). As a consequence, the dominant orbital nature in the hole pocket changes from Fe $3d_{yz/zx}$ in CaFeAsF, to Fe $3d_{x^2-y^2}$ and $3d_{z^2}$ in CaFeAsH. Figure 3(c) shows the Fermi surfaces of CaFeAsH and CaFeAsF. They each have two hole pockets (denoted as α_2 and γ) and two electron pockets with the same orbital nature. The primary difference between them is the shape of the smallest hole pocket (denoted as α_1) around the Γ-Z line, which is indicated by the red line. A sandglass-shaped pocket exists in CaFeAsH, compared with a cylinder-shaped pocket in CaFeAsF. Figure 4 shows the Fermi surfaces of $CaFe_{1-x}Co_xAsH$ and $CaFe_{1-x}Co_xAsF$, with $x = 0.10$ which corresponds to the optimal electron doping level. As described in the Supplemental Material (Figs. S1 and S2 of [29]), a rigid band model is valid for Co substitution. That

is, the band structure of $CaFe_{1-x}Co_xAs(H, F)$ is similar to that of CaFeAs(H, F), with the E_F shift corresponding to the number of electrons supplied from Co. The E_F shift results in the smallest hole pockets in both systems remaining largely unchanged by Co doping. However, two hole pockets diminish and two electron pockets slightly enlarge with increasing Co content. This robustness of the α_1 hole pocket against Co doping is attributed to the dispersion of the band producing the α_1 hole pocket being larger than that of the electron, α_2, or γ hole pocket.

IV. DISCUSSION

The difference in the electronic structures of CaFeAsH and CaFeAsF is first discussed. The differences in the calculation are the structural parameters (a, c, z_{As}, and z_{Ca}) and the anion species within the blocking layer (H$^-$ or F$^-$). However, the band structure calculated for CaFeAsF using the structural parameters for CaFeAsH does not reproduce the Fe $3d$ band crossing the E_F in the Γ-Z path (See Supplemental Material, Fig. S3 of [29]). Therefore, the three-dimensional (3D) nature originates from the contribution of the hydrogen $1s$ state, despite it being located far from the E_F. Figure 3(a) shows that the hydrogen $1s$ states energetically overlap well with As $4p$, and slightly overlap with the Ca components. The fluorine $2p$ states do not energetically overlap with the Ca components. This overlap results in the formation of weak covalent bonding. The covalency of energetically overlapped H $1s$ and As $4p$ states is investigated next. Figure 5(a) shows the contribution of As $4p$ and H $1s$ to the band dispersion. In CaFeAsH, hybridization of As $4p$ with the H $1s$ orbital is apparent in some parts of the bands. This indicates the presence of covalent bonding between them, despite their being separated by 334 pm. No such covalency is observed in CaFeAsF, because each orbital contribution is distinctly separated between F $2p$ and As $4p$ states.

The effect of this covalent bonding on the Fermi surface is discussed next. The change in the band structure of CaFeAsH near the E_F is explained by the schematic orbital configuration
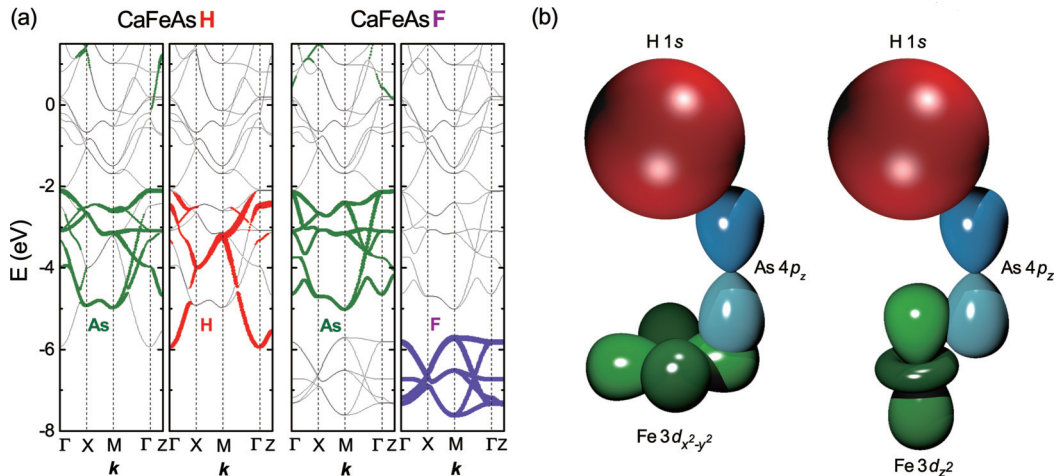

FIG. 5. (Color online) Contribution of arsenic, hydrogen, and fluorine atomic orbitals to the electronic structures of CaFeAsH and CaFeAsF. (a) Thickness of bands shows the amounts of As p (green), H $1s$ (red), and F $2p$ (purple) character. (b) and (c) Schematics showing the configurations of the H $1s$, As $4p$, Fe $3d_{x^2-y^2}$, and $3d_{z^2}$ orbitals.

shown in Fig. 5(b). The H $1s$ orbital covalently bonds with the As $4p_z$ orbital, the latter of which is overlapped with the lobes of the Fe $3d_{x^2-y^2}$ and $3d_{z^2}$ orbitals. The H $1s$ orbital weakly overlaps with Ca $4s/3d$ orbitals. The As $4p$ orbitals mediate the interlayer bonding of the Fe $3d_{x^2-y^2}$ and $3d_{z^2}$ orbitals in adjacent FeAs layers. This results in the 3D electronic structure observed in Fig. 3(b). The dispersion of As $4p_z$-derived bands along the Γ-Z direction depends on the dimensionality of the crystal structure [30]. For example, the bandwidth along Γ-Z is ≈ 0 eV in $Ca_4As_2O_6Fe_2As_2$ with its thick blocking layer, while it is 0.4 and 2 eV in LaFeAsO and $BaFe_2As_2$, respectively. In $BaFe_2As_2$, the energy band with Fe $3d_{z^2}$ character crosses the E_F, forming the 3D hole pocket. The 3D electronic nature of $BaFe_2As_2$ is apparent from its electron transport properties [31]. In CaFeAsH, the 3D electronic nature is caused by bonding passing through the As-H-Ca bond. Covalent bonding between H and As is also reflected in the crystal structure of CaFeAsH: The shorter d_{Ca-As} distance in $CaFe_{1-x}Co_xAsH$ in Fig. 1(e) results from the decreased As-H separation. Electrons in the As $4p_z$ orbital are partly utilized in bond formation. Thus, the Fe-As bond in CaFeAsH weakens and lengthens relative to that in CaFeAsF, as shown in Fig. 1(g).

Spin fluctuations arising from the Fermi surface nesting between the hole and electron pockets are a plausible explanation for the mediation of superconductivity in iron pnictides [32,33]. The primary difference in the Fermi surfaces of CaFeAsH and CaFeAsF is the dimensionality of the α_1 hole pocket around the Γ-Z line, as indicated by the red line. The former is 3D and the latter is two dimensional (2D). Both hole pockets are smaller, and their curvatures are much larger than those of the electron pockets. This means the α_1 hole pocket does not contribute effectively to the nesting, i.e., the development of spin fluctuation. The size and shape of the α_1

hole pocket remain largely unchanged up to $x = 0.1$, indicating that its contribution to superconductivity is small.

This hydrogen effect leads us to further consider its role in hydrogen-substituted LnFeAsO. Hydrogen substitution effectively forms 3D Fermi surfaces, even for materials with 2D crystal structures. However, this change in Fermi surface does not affect their superconducting properties. Hydrogen is an effective dopant for electron generation via oxygen site substitution, similarly to fluorine in LnFeAsO. This indicates that incorporating hydrides enhances the 3D nature of 1111-type compounds, without suppressing their superconductivity.

V. SUMMARY

Superconductivity was observed in $CaFe_{1-x}Co_xH$, and its properties were compared with those of $CaFe_{1-x}Co_xAsF$. The maximum T_c and width of the superconducting dome of $CaFe_{1-x}Co_xAsH$ are almost the same as those of $CaFe_{1-x}Co_xAsF$. The calculated electronic structure of CaFeAsH differs from that of CaFeAsF. The former has a 3D hole surface, with a highly 3D nature. This fact is caused by covalent bonding between energetically overlapped As $4p$ and H $1s$ bands. This 3D hole surface does not interfere with superconductivity because poor nesting between this small hole surface and electron surfaces causes the unfavorable development of excitations, such as spin and/or charge. Hydrogen incorporated within the blocking layer acts as an indirect electron dopant, without interfering with the superconductivity.

ACKNOWLEDGMENT

[1] Y. Kamihara, T. Watanabe, M. Hirano, and H. Hosono, J. Am. Chem. Soc. **130**, 3296 (2008).

[2] M. Rotter, M. Tegel, and D. Johrendt, Phys. Rev. Lett. **101**, 107006 (2008).

[3] J. H. Tapp, Z. Tang, B. Lv, K. Sasmal, B. Lorenz, P. C. W. Chu, and A. M. Guloy, Phys. Rev. B **78**, 060505 (2008).

[4] X. Zhu, F. Han, G. Mu, P. Cheng, B. Shen, B. Zeng, and H.-H. Wen, Phys. Rev. B **79**, 220512 (2009).

[5] H. Ogino, Y. Matsumura, Y. Katsura, K. Ushiyama, S. Horii, K. Kishio, and J. Shimoyama, Supercond. Sci. Technol. **22**, 075008 (2009).

[6] F.-C. Hsu, J.-Y. Luo, K.-W. Yeh, T.-K. Chen, T.-W. Huang, P. M. Wu, Y.-C. Lee, Y.-L. Huang, Y.-Y. Chu, D.-C. Yan, and M.-K. Wu, Proc. Natl. Acad. Sci. USA **105**, 14262 (2008).

[7] J. Guo, S. Jin, G. Wang, S. Wang, K. Zhu, T. Zhou, M. He, and X. Chen, Phys. Rev. B **82**, 180520 (2010).

[8] X. H. Chen, T. Wu, G. Wu, R. H. Liu, H. Chen, and D. F. Fang, Nature **453**, 761 (2008).

[9] R. Zhi-An, L. Wei, Y. Jie, Y. Wei, S. Xiao-Li, Zheng-Cai, C. Guang-Can, D. Xiao-Li, S. Li-Ling, Z. Fang, and Z. Zhong-Xian, Chin. Phys. Lett. **25**, 2215 (2008).

[10] G. F. Chen, Z. Li, D. Wu, G. Li, W. Z. Hu, J. Dong, P. Zheng, J. L. Luo, and N. L. Wang, Phys. Rev. Lett. **100**, 247002 (2008).

[11] Z.-A. Ren, J. Yang, W. Lu, W. Yi, X.-L. Shen, Z.-C. Li, G.-C. Che, X.-L. Dong, L.-L. Sun, F. Zhou, and Z.-X. Zhao, Europhys. Lett. **82**, 57002 (2008).

[12] S. Matsuishi, Y. Inoue, T. Nomura, H. Yanagi, M. Hirano, and H. Hosono, J. Am. Chem. Soc. **130**, 14428 (2008).

[13] S. Matsuishi, Y. Inoue, T. Nomura, M. Hirano, and H. Hosono, J. Phys. Soc. Jpn. **77**, 113709 (2008).

[14] A. S. Sefat, A. Huq, M. A. McGuire, R. Jin, B. C. Sales, D. Mandrus, L. M. D. Cranswick, P. W. Stephens, and K. H. Stone, Phys. Rev. B **78**, 104505 (2008).

[15] C. Wang, Y. K. Li, Z. W. Zhu, S. Jiang, X. Lin, Y. K. Luo, S. Chi, L. J. Li, Z. Ren, M. He, H. Chen, Y. T. Wang, Q. Tao, G. H. Cao, and Z. A. Xu, Phys. Rev. B **79**, 054521 (2009).

[16] G. Cao, S. Jiang, X. Lin, C. Wang, Y. Li, Z. Ren, Q. Tao, C. Feng, J. Dai, Z. Xu, and F.-C. Zhang, Phys. Rev. B **79**, 174505 (2009).

[17] Y. K. Li, X. Lin, T. Zhou, J. Q. Shen, Q. Tao, G. H. Cao, and Z. A. Xu, J. Phys. Condens. Matter **21**, 355702 (2009).

[18] T. Hanna, Y. Muraba, S. Matsuishi, N. Igawa, K. Kodama, S. I. Shamoto, and H. Hosono, Phys. Rev. B **84**, 024521 (2011).

[19] S. Matsuishi, T. Hanna, Y. Muraba, S. W. Kim, J. E. Kim, M. Takata, S. I. Shamoto, R. I. Smith, and H. Hosono, Phys. Rev. B **85**, 014514 (2012).

[20] S. Iimura, S. Matuishi, H. Sato, T. Hanna, Y. Muraba, S. W. Kim, J. E. Kim, M. Takata, and H. Hosono, Nat. Commun. **3**, 943 (2012).

[21] H. Soeda, H. Takahashi, T. Tomita, S. Matsuishi, T. Hanna, Y. Muraba, and H. Hosono, Meeting Abstracts of the Physical Society of Japan (in Japanese) **68**(1), 712, Pt. 3 (2013).

[22] Y. Fukai and N. Ōkuma, Jpn. J. Appl. Phys. **32**, L1256 (1993).

[23] TOPAS, Version 4.2 (Bruker AXS, Karlsruhe, Germany, 2009).

[24] J. P. Perdew, K. Burke, and M. Ernzerhof, Phys. Rev. Lett. **77**, 3865 (1996).

[25] J. P. Perdew, K. Burke, and M. Ernzerhof, Phys. Rev. Lett. **78**, 1396 (1997).

[26] P. E. Blöchl, Phys. Rev. B **50**, 17953 (1994).

[27] G. Kresse and J. Furthmüller, Phys. Rev. B **54**, 11169 (1996).

[28] $CaFe_{1-x}Co_xAsF$ were prepared by solid-state reaction of CaF_2, CaAs, Fe_2As, and Co_2As in an evacuated silica tube at 1273 K. The samples were ground into a powder and placed in a glass capillary ($\phi = 0.5$ mm), and XRD using Mo $K\alpha$ radiation at room temperature was measured by transmission mode. Their structure parameters were obtained by the Rietveld analysis of XRD patterns.

[29] See Supplemental Material at http://link.aps.org/supplemental/10.1103/PhysRevB.89.094501 for calculated electronic structures of $CaFe_{1-x}Co_xAsF$ and $CaFe_{1-x}Co_xAsH$.

[30] H. Usui, K. Suzuki, and K. Kuroki, Supercond. Sci. Technol. **25**, 084004 (2012).

[31] T. Katase, S. Iimura, H. Hiramatsu, T. Kamiya, and H. Hosono, Phys. Rev. B **85**, 140516 (2012).

[32] I. I. Mazin, D. J. Singh, M. D. Johannes, and M. H. Du, Phys. Rev. Lett. **101**, 057003 (2008).

[33] K. Kuroki, S. Onari, R. Arita, H. Usui, Y. Tanaka, H. Kontani, and H. Aoki, Phys. Rev. Lett. **101**, 087004 (2008).